ChemCatChem

Research Article
doi.org/10.1002/cctc.202500859

Chemistry Europe
European Chemical
Societies Publishing

www.chemcatchem.org

Role of Gas Dropouts in CO_2 Methanation over MOF-Derived Ni_3Fe@C Catalysts: An In Situ XAS and PDF Study

Fabio Manzoni,[a] Sven Strübbe,[b] Leif Rohrbach,[c] Maxime Boniface,[d] Thomas Lunkenbein,[d] Roland Schoch,[b] Wolfgang Kleist,[c] Matthias Bauer,*[b] and Mirijam Zobel*[a, e]

With industrial chemical processes facing the challenges of renewable energy supply, catalysts are needed that withstand fluctuations of operating conditions. For methanation reactions using hydrogen from electrocatalytic water splitting, dropouts of hydrogen are amongst the realistic scenarios. While Ni-based catalysts are the most widely used, bimetallic Ni/Fe-based catalysts recently emerged as superior. A new method of preparing highly active metallic catalysts is the decomposition of metal-organic frameworks. Even though it is difficult to control the particle size distribution and the homogeneity of the formed nanoparticles with this method, the carbonaceous features present between the nanoparticles permit avoiding the use of support, leading to a high-loading catalyst with superior stability. Here, we investigate with in situ X-ray absorption spectroscopy and pair distribution function analysis the structural details of a Ni_3Fe@C methanation catalyst derived from a metal-organic framework during its activation and catalysis under H_2-dropout conditions. Despite the similarity of these phases, it was possible to identify two fcc phases of Ni_3Fe and Ni coexisting during catalytic cycling, with a Fe_2NiO_4 spinel phase appearing during dropouts. This indicates oxidation of the particle surface in the absence of hydrogen, which can be fully recovered by reactivation in pure hydrogen atmosphere, providing high stability of the catalyst during an industrially relevant dropout scenario.

1. Introduction

For the transition toward a sustainable economy based on renewable energies, base chemicals such as methane need to be produced from renewable sources. The methanation of carbon dioxide can be described by the reverse water–gas shift reaction (Equation 1) followed by the subsequent methanation of carbon monoxide (Equation 2).[1,2]

$$CO_2 + H_2 \rightleftharpoons CO + H_2O \tag{1}$$

$$CO + 3H_2 \rightleftharpoons CH_4 + H_2O \tag{2}$$

To run this reaction renewably, carbon dioxide can be gained via direct air capture or other capture processes and hydrogen from electrocatalytic water splitting. Nickel catalysts play a major role for the methanation reaction because of their low cost and high natural abundance, being industrially employed supported on alumina, for instance.[3] Catalysts derived from metal-organic frameworks (MOFs) via their controlled thermal decomposition have appeared as an alternative route to nanostructured catalysts for use in, e.g., Fischer–Tropsch synthesis.[4–6] Hereby, the metallic nodes of the MOF can result in well-dispersed metal nanoparticles within carbonaceous shells.[4–6] The decomposition conditions (inert, non-oxidative, or reducing gas atmospheres as well as temperature) play a major role in the control of the particle size, morphology, and carbon content of the MOF-derived compounds, as shown, for example, on Fe-MIL-127,[7] Cu-BTC (HKUST-1),[8] or a Ni(BDC)(PNO)-MOF.[9] The carbonaceous shells of these MOF-derived catalysts are hypothesized to contribute to their enhanced stability during catalytic cycling. For a Ni@C catalyst consisting of Ni nanoparticles in a carbonaceous shell, derived from Ni(BDC)(PNO), we have investigated the impact of different gas dropout conditions in the methanation reaction on the catalyst stability and activity via in situ X-ray absorption spectroscopy (XAS) and total scattering

---

[a] F. Manzoni, M. Zobel
Institute of Crystallography, RWTH Aachen University, Aachen 52066, Germany
E-mail: zobel@ifk.rwth-aachen.de

[b] S. Strübbe, R. Schoch, M. Bauer
Department of Chemistry and Center for Sustainable Systems Design (CSSD), Paderborn University, Paderborn 33098, Germany
E-mail: bauerm@mail.uni-paderborn.de

[c] L. Rohrbach, W. Kleist
Department of Chemistry, RPTU Kaiserslautern-Landau, Kaiserslautern 67663, Germany

[d] M. Boniface, T. Lunkenbein
Department of Inorganic Chemistry, Fritz-Haber-Institut der Max-Planck-Gesellschaft, Berlin 14195, Germany

[e] M. Zobel
JCNS-3: Neutron Analytics for Energy Research, Forschungszentrum Jülich GmbH, Wilhelm-Johnen-Straße 52428, Jülich, Germany

Supporting information for this article is available on the WWW under https://doi.org/10.1002/cctc.202500859

Research Article
doi.org/10.1002/cctc.202500859

experiments with subsequent analysis of the pair distribution function (PDF).[10] Three different types of dropout scenarios were investigated: a) full hydrogen loss, b) partial hydrogen dropout by 50%, and c) reduction of H_2 and CO_2 flows keeping their stoichiometric relation constant. The stoichiometric reduction showed the highest catalyst activity over 24 h compared to the other dropout scenarios, keeping the carbon shell around the Ni nanoparticles intact.[10]

Despite the fact that the combination of XAS and PDF studies has emerged as a highly effective approach to elucidate the structural characteristics of disordered nanoparticles, this methodological amalgamation remains scarcely utilized in in situ and operando studies of heterogeneous catalysts.[11,12] XAS is a dedicated method to investigate the local structure in terms of type, number, and distance of coordinating neighbors around an X-ray absorbing atom up to a realistic limit of 5 Å by extended X-ray absorption fine structure (EXAFS) analysis. Moreover, this information can be obtained in an element-specific manner predestined for the analysis of mixed metal compounds. Additionally, the oxidation state of the investigated metal can be probed by X-ray absorption near edge structure (XANES).[13,14] The PDF complements the short-range order with distances of ~1 Å, but add the medium- or long-range order of several tenths of nanometers, yet being not element-sensitive.[15] In recent years in the field of heterogeneous catalysis, PDF measurements accessed, for instance, the local disorder and size of supported catalytic clusters and nanoparticles,[16] even with laboratory PDF data only,[17] and in situ experiments could follow the formation and structural evolution of catalytic particles during activation and catalytic cycling.[18,19]

Bimetallic NiFe catalysts have been shown to be promising candidates to alleviate the insufficient low-temperature activity and deactivation encountered in Ni methanation catalysts.[20,21] Iron can easily form alloys with Ni, resulting in an expansion of the Ni_{fcc} lattice, while for high Fe contents, the bcc lattice of pure Fe can be adopted.[20] The formed NiFe alloys remain intact during the reaction and provide a synergistic effect, which lowers the energy barrier for methane formation.[22–24] For instance, XAS found the formation of surface FeO_x clusters on top of the bimetallic Ni—Fe particles during catalyst activation with a highly dynamic redox process in iron activating CO_2 by promoting its hydrogenation to formate intermediates, which are crucial in the methanation pathway as found by density functional theory simulations.[25–28]

In analogy to our Ni@C catalyst studies, catalytic tests have revealed a superior catalyst stability of a Ni_3Fe@C MOF-derived methanation catalysts during full hydrogen dropout conditions in catalytic cycling. Hence, here we combine in situ XAS and PDF experiments to reveal the structural changes of the catalyst during activation, methanation and full dropout conditions.

2. Results and Discussion

2.1. Catalytic Tests

In line with other works highlighting the particular role of the Ni_3Fe composition on Al_2O_3 and SiO_2 supports[29–31] and in line with theoretical predictions on the optimum Ni/Fe ratios,[32] the composition of Ni_3Fe is favorable in MOF-derived catalysts for the catalytic performance of CO_2 methanation compared to higher iron fractions.[33] Hence, here we investigate the catalytic performance of a Ni_3Fe@C (determined molar Ni/Fe ratio = 3.35:1; total metal content: 70 wt %) catalyst obtained by decomposition of a MIL-53-derived Ni,Fe-MOF at 500 °C in 10% H_2/He for 1 h. The full details of the standard characterization for this catalyst, as well as an in-depth study on its catalytic behavior and stability in the methanation of carbon dioxide under dynamic conditions in a lab setup are reported elsewhere.[33] For the catalytic characterization, we study two dynamic operation conditions simulating full and partial dropouts in comparison to static conditions.[10] For the dropout scenarios, a cycle duration of 30 min was applied. The investigated catalyst is highly active in the methanation of CO_2. Under static methanation conditions (see Figure 1a,d), the CO_2 consumption rate and the methane production rate are decreasing over time, and the selectivity shifts toward carbon monoxide. A comparable behavior can be observed under partial dropout conditions (see Figure 1b,e). At the beginning of the experiment, the consumption rate of CO_2 decreases for the first 5 h and then remains nearly constant. The methane production rate is slightly decreasing over time, and the selectivity shifts toward carbon monoxide. During the dropouts, more carbon monoxide is produced at the cost of the methane production rate, as the reaction stoichiometry is altered. A completely different behavior can be observed during the experiment under full H_2 dropout conditions (see Figure 1c,f). The full H_2 dropout scenario revealed the best catalytic stability for a time on stream of 24 h. The catalyst exhibits a strong activation behavior after the first dropout and a high CO_2 consumption rate between the dropouts. In between the first 3–4 dropouts, the CO_2 consumption rate is still increasing and then decreases only slightly over time from 0.36 mmol min^{-1} in the second cycle to 0.30 mmol min^{-1} in cycle 24 (see Figure 1c). After each full H_2 dropout, the CO_2 consumption rate and the methanation production rate are nearly full restored. The CH_4 selectivity stays as high as 89% (Figure 1f).

2.2. PXRD and PDF Analysis

The fits of the in situ PDF data measured during the catalyst activation (400 °C in H_2 atmosphere) require three phases to model the data: one Fe_{bcc} phase and two fcc phases (Ni_{fcc} and Ni_3Fe_{fcc}), see Figure 2a,b. Due to the similarity in the crystal structure of the Ni_3Fe alloy and bulk Ni_{fcc} or bulk Fe_{fcc} phases, it is difficult to discriminate the alloy from the metallic phases in the PXRD data. In the PDF, too, the first metal-metal interatomic distances are very similar with 2.49 Å for Ni_{fcc}, 2.54 Å for Fe_{fcc}, and 2.51 Å for Ni_3Fe_{fcc}.[34] The fitted lattice parameter of the phase is $a = 3.535$ Å for $t = 0$ h, and since this value is closer to the bulk Ni_{fcc} lattice parameter of 3.525 Å than to the bulk Fe_{fcc} one of 3.591 Å,[35] we labeled this phase Ni_{fcc}. Yet, an absolute distinction just based on the lattice parameter is not possible, as internal strain can further modify the nanoparticles, and Fe is known to form Fe-rich surface layers on NiFe alloy particles,[36] result-

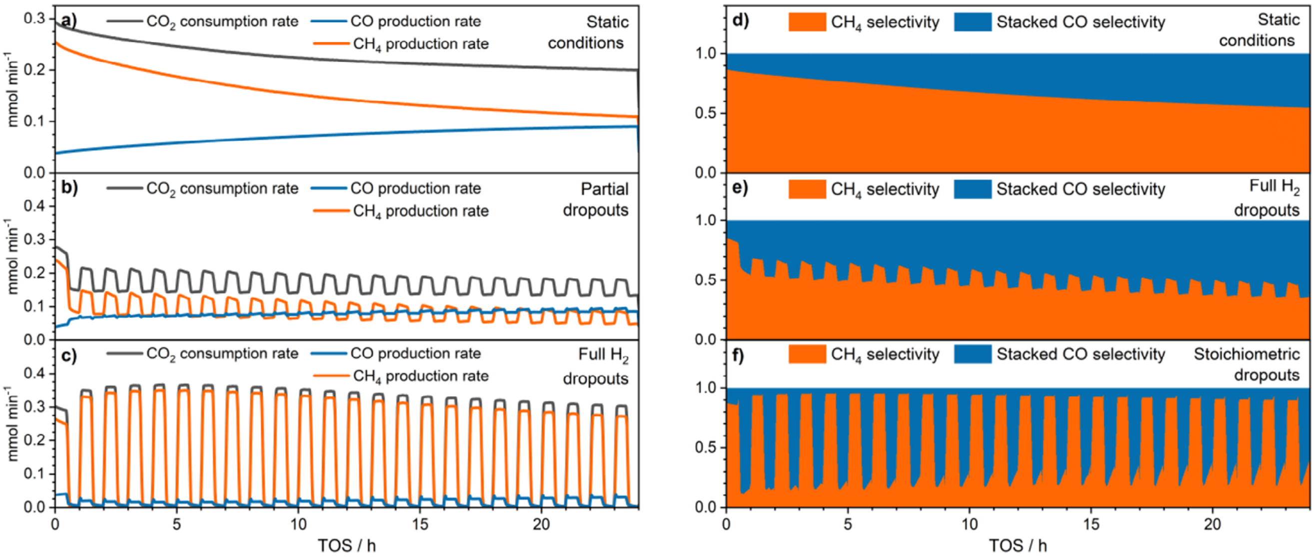

Figure 1. CO_2 methanation catalyzed by $Ni_3Fe@C$ under static CO_2 methanation conditions a), d) and different dynamic operating conditions b), c), e), f). Every 30 min, the reaction conditions were switched between methanation conditions (66 mL min^{-1} N_2:H_2:CO_2 = 0.5:4:1), full H_2 dropout conditions c), f), and partial H_2 dropout conditions b), e). The reaction was performed at 425 °C and 1 atm.

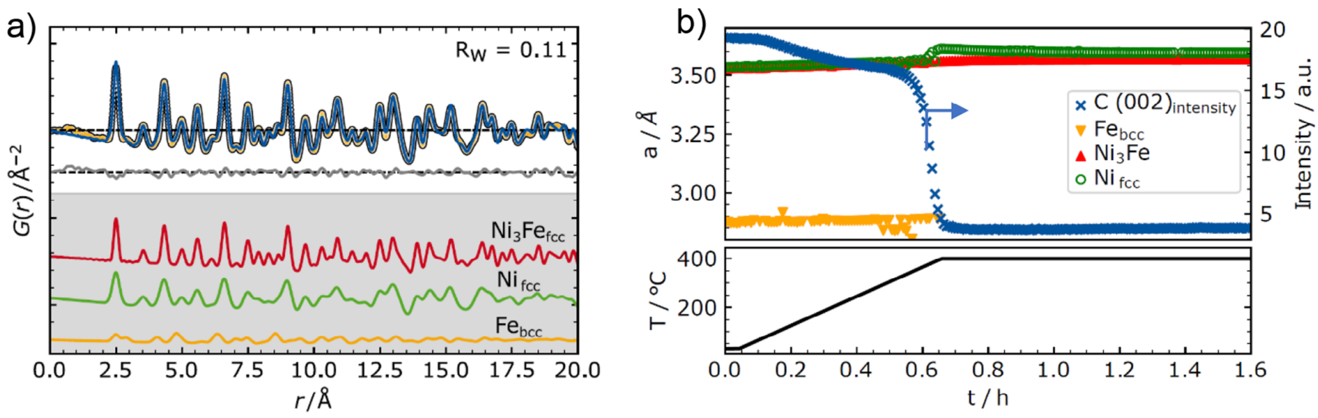

Figure 2. Activation: a) representative PDF refinement during the activation process (400 °C, H_2 atmosphere) for $t = 0$ min; b) intensity of the graphite Bragg peak (002) from PXRD, and refined lattice parameters from PDF refinements for the three phases Fe_{bcc} (yellow triangle), Ni_{fcc} (green circle), and Ni3Fe alloy (red triangle) as a function of time, together with the temperature ramp in the bottom panel.

ing in a variation of composition and lattice parameters within individual nanoparticles. The second phase we labelled Ni_3Fe_{fcc}, because TEM measurements with EDX maps further helped in confirming the existence of the alloy phase, see the co-existence of Ni and Fe in the same regions in Figures S6 and S7. Further, ICP-OES measurements confirm the Ni_3Fe composition. Figure 2a shows the PDF fit for $t = 0$ h over the r range up to 20 Å and Figure S3 for the full r range, while Figure S4 shows a PDF refinement for $t = 1.5$ h.

During the heating ramp of the activation for T <400 °C, the two fcc phases (Ni and Ni_3Fe) have similar lattice parameters of ~3.53 Å, but different particle diameters of about 6 and 14 nm, see Table S1 for the PDF fit results of lattice parameters, scale factors, and particle diameters. Those PDF-derived particle diameters are an ensemble average and correspond to crystalline domain diameters. An additional bcc Fe phase of 16 nm particles is coexisting during heating up to 400 °C, which disappears entirely when the final temperature of 400 °C is reached, see Figure 2b.

Upon this, there is a noticeable increase in the Ni_{fcc} lattice parameter to 3.613 Å and an increase in the particle diameter to 9 nm. Keeping the temperature at 400 °C for 1 h, the lattice parameter of this phase decreases from 3.613 to 3.594 Å, matching the bulk Fe_{fcc} lattice parameter.[35] The lattice parameter of the Ni_3Fe_{fcc} phase increases less, but gradually up to 3.57 Å, indicating the formation of an iron-rich alloy phase, which has a larger lattice parameter compared to Ni_3Fe.[36,37] The corresponding nanoparticle diameter increases only slightly from 14 to about 16 nm. Hence, at the end of the activation, both fitted fcc phases have increased in average domain size and are likely alloy phases, one being more Fe-rich than the other.

Figure 2b further reveals that the graphitic shell of the NiFe@C catalyst particles gets increasingly decomposed with increasing temperature during activation in a reducing atmo-

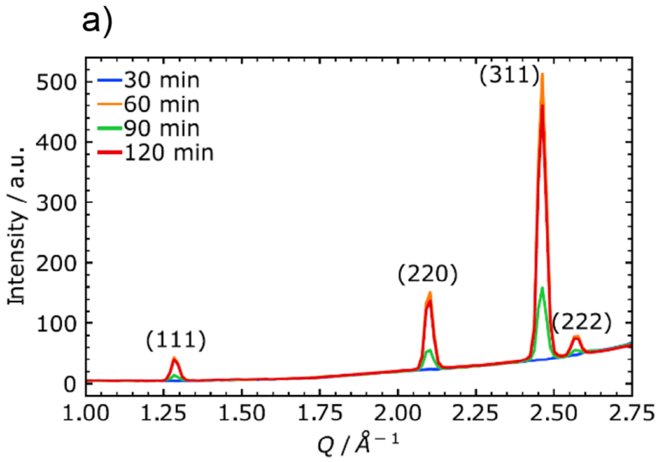

Figure 3. a) Bragg peaks of Fe_2NiO_4 during the first two methanation and dropout cycles. b) Intensity variation of the (311) Fe_2NiO_4 Bragg peak during catalytic cycling: green areas represent the methanation condition (labeled m), the white areas represent the dropout (labeled d), and the red area represents the reactivation of the catalyst.

sphere, as deduced from the decreasing integral intensity of the (002) Bragg peak of graphite. Shortly before reaching 400 °C, the graphitic Bragg peak vanishes almost completely. With the disappearance of the graphitic Bragg peak, the Fe_{bcc} phase disappears concurrently, which points toward a stabilizing effect of the graphitic shell for the Fe_{bcc} particles.

Complementary EDX maps of the samples after activation (Figure S6) and post catalytic investigation (Figure S7) confirm that the carbon shell around the nanoparticles disintegrates. Some carbon remains, mainly in between few particles. This does not contradict the low intensity of the graphitic Bragg peak, because disintegrated, very disordered carbon residuals would produce very diffuse, background-like scattering instead of Bragg peaks. Though the samples studied by TEM stem from the catalytic tests in the laboratory setup, which may result in somewhat different sample morphology compared to the flow cells optimized for in situ synchrotron experiments.

In conclusion, we propose that the disintegration of the graphitic shells, which stabilize the Fe_{bcc} nanoparticles, results in the transformation of Fe_{bcc} into Fe_{fcc}. Because of the high structural similarity between Ni_{fcc}, Fe_{fcc}, and alloy phases, it cannot be derived from these PXRD/PDF data, whether Fe_{fcc} particles coexist with Ni_{fcc} particles, resulting in the observed average lattice parameters, or whether a strong immediate alloy formation sets in upon the Fe_{bcc} disintegration. Since the lattice parameter of the Ni_{fcc}-labeled phase decreases within 0.3 h after Fe_{bcc} disintegration and then runs into a plateau, this points toward an ongoing alloy formation. At first, the Fe and Ni could be spatially more distributed, with the Fe domains increasing the apparent average lattice parameter. Over time at 400 °C, Fe diffuses deeper into the already existing Ni particles, resulting in a more homogeneous alloy with a slightly smaller lattice parameter.

During the catalytic cycling of the catalyst at the beamline between methanation and full dropout conditions, its high catalytic activity toward methanation, as observed in the laboratory experiment, was confirmed. We found a dropout-dependent formation of a spinel phase (Fe_2NiO_4), visible in the PXRD patterns shown in Figure 3a. During the first full dropout cycle, in the absence of H_2, new Bragg peaks appear at Q values of 1.30, 2.13, 2.45, and 2.58 $Å^{-1}$, see Figure 3a (being a zoom into the low Q range of the full PXRD patterns shown in Figure S2). These peaks can clearly be attributed to the spinel Fe_2NiO_4, which has been observed before via HR-TEM on the surface of NiFe alloy particles.[36] Figure 3b shows that this Fe_2NiO_4 phase increases in amount during all dropouts, while its fraction decreases during methanation conditions (see also the oscillation of the Bragg peaks in the heat map in Figure S1). This oscillatory trend can be explained by the fact that the oxidizing environment during the dropout condition oxidizes the surface metal atoms of the alloy particles. During methanation in the presence of hydrogen, a partial reduction of this oxidized layer takes place, although not all of the spinel can be reduced.

Switching to reactivation conditions after seven cycles, i.e., pure hydrogen atmosphere, promptly reduces all spinel and recovers the alloy and fcc phases. Since we had observed a fast deactivation of the monometallic MOF-derived Ni@C catalyst in full dropout scenarios,[9] we assume that the formation of this oxide layer protects the active site of the catalyst against fast deactivation, leading to a more stable and active catalyst for full dropout conditions. This high stability of the Ni_3Fe alloy is even more to be pointed out, as the graphitic shells of the $Ni_3Fe@C$ catalyst strongly disintegrate during activation and turn rather into carbon residuals in between particles.

2.3. XAS Analysis

The results achieved by total scattering are supported and can be extended by X-ray absorption spectroscopy (XAS). Analysis of the XANES region gives information about the energy and shape of the absorption edge and thus about the oxidation state of the absorbing atom.

All spectra obtained through measurements at the Ni K-edge (8333 eV, shown in Figure S8) from the catalyst in situ after activation and during several methanation and full dropout scenarios show only marginal differences and indicate a very stable cata-

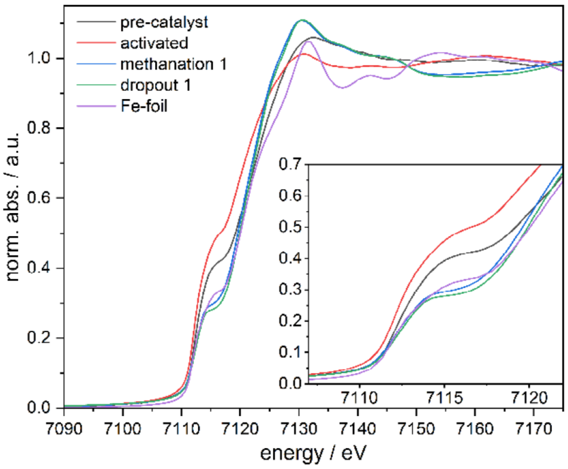

Figure 4. In situ XANES spectra of the catalyst (at the Fe K-edge) at different stages during activation and the first methanation/full dropout cycle.

lyst species in a metallic oxidation state. It has to be mentioned that a possible minor formation of a Fe—Ni alloy, as indicated by total scattering, cannot be resolved by XAS, since the average spectral signal of all Ni species is always detected.

Due to the bimetallic composition of the catalyst, the same reactions were also followed at the Fe K-edge (7112 eV) under identical conditions. The corresponding spectra are shown in Figure 4 before and after activation as well as after application in the first methanation/full dropout scenario in comparison to a spectrum of metallic iron. It is clearly visible that the pre-catalyst is reduced during the activation treatment forming oscillations comparable to the ones from metallic iron, but with rather small particle size as deduced from the broadened spectrum. Under methanation conditions, the iron centers are oxidized even to a larger extent as in the pre-catalyst, as can be seen from the shift of the absorption edge position to higher energies, the formation of a less-intense pre-edge feature, and a more pronounced white line intensity. In the course of a full hydrogen dropout scheme the changes are less pronounced but still indicating a progressing oxidation of the catalyst. These findings fit very well to the results obtained by powder XRD and PDF measurements, where a spinel phase (Fe_2NiO_4) was found during methanation, which possibly forms at the particle surface. By comparing the spectra acquired during seven methanation/full dropout cycles shown in Figure 5, a weak overall oxidation can be observed, leading to the conclusion that the amount of spinel phase increases slowly over time, as already indicated by PDF. Through reactivation, the initial spectrum after the first activation could be recovered completely, as shown in Figure 6. In the following two cycles of methanation and full hydrogen dropout were carried out, and the spectra under 'methanation-after-reactivation' conditions (mar 1 and mar 2) were measured. While the spectrum of mar 1 shows only slight signs of oxidation compared to the reactivated spectrum, the second spectrum mar 2 is comparable to the spectrum obtained after the first methanation. The changes of the catalyst spectra progress, therefore, slower after reactivation.

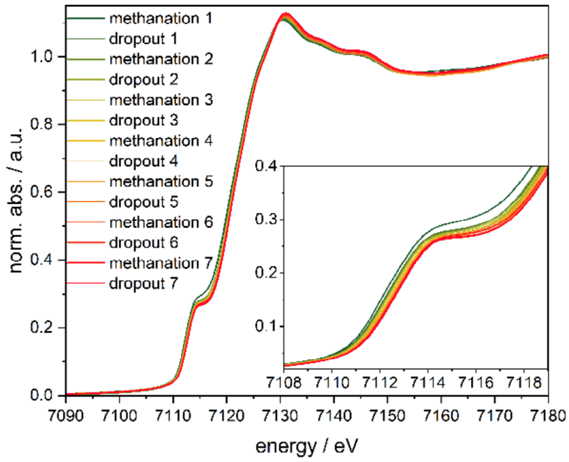

Figure 5. In situ XANES spectra of the catalyst at the Fe K-edge during seven methanation/full dropout cycles scenarios.

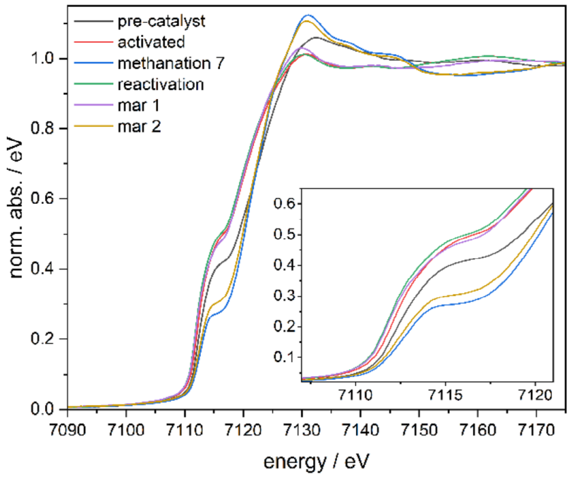

Figure 6. In situ XANES spectra of the catalyst at the Fe K-edge comparing spectra before and after reactivation.

In order to obtain more detailed information about structural changes, an EXAFS analysis of the measured in situ spectra was carried out. Due to the variety of different phases and species present in the system and the quality of the spectra, the analysis was performed using Fourier filtering (see Table 1). The measurements under in situ conditions caused on the one hand, the necessity to use undiluted catalyst (and with this a high metal concentration) and, on the other hand, measurements in fluorescence mode. Both facts lead to a significant self-absorption resulting in dampened oscillations in the EXAFS region and reduced values for the obtained numbers of backscatterers (Figure 7). Since the metal concentration and measurement geometry did not change during the experiment, a qualitative comparison between the spectra is still possible.

To fit the spectra, a model was established that includes possible backscatterers of the Fe_2NiO_4 spinel phase indicated by PXRD and pure bulk metal phase. Typical distances were extracted from single-crystal data as a starting point and refined afterwards. Two oxygen shells were adjusted at distances of 1.9 and 2.0 Å accounting for tetrahedral and octahedral coor-

Table 1. Structural parameters obtained by fitting the experimental spectra of the in situ measurement at the Fe K-edge.

Abs-Bs[a]	N(Bs)[b]	R(Abs-Bs)[c]/Å	σ^2 [d]/Å^2	R[e] /%, χ_{red}^2[f], E_f[g]/eV, Afac[h]
Pre-catalyst			FF-range: 1.1–4.2 Å[i]	
Fe—O	0.4 ± 0.1	1.849 ± 0.018	0.032 ± 0.003	5.623
Fe—O	0.5 ± 0.1	1.977 ± 0.019	0.032 ± 0.003	1.31×10^{-6}
Fe—Fe	3.0 ± 0.3	2.481 ± 0.025	0.067 ± 0.007	−4.021
Fe—Fe/Ni	1.9 ± 0.2	2.837 ± 0.028	0.100 ± 0.010	0.800
Fe—Fe	1.2 ± 0.1	3.452 ± 0.035	0.087 ± 0.009	
Fe—Fe	1.2 ± 0.1	3.978 ± 0.039	0.055 ± 0.006	
Activation			FF-range: 1.1–4.2 Å[i]	
Fe—Fe	2.4 ± 0.1	2.464 ± 0.025	0.081 ± 0.008	10.21
Fe—Fe/Ni	1.1 ± 0.1	2.887 ± 0.029	0.112 ± 0.011	1.47×10^{-6}
Fe—Fe	1.2 ± 0.1	3.515 ± 0.035	0.112 ± 0.011	−4.109
Fe—Fe	0.4 ± 0.1	4.006 ± 0.040	0.050 ± 0.005	0.800
Methanation 1			FF-range: 1.1–3.6 Å[i]	
Fe—O	1.8 ± 0.1	1.914 ± 0.019	0.095 ± 0.010	10.86
Fe—O	0.4 ± 0.1	2.077 ± 0.021	0.032 ± 0.003	3.10×10^{-6}
Fe—Fe	1.1 ± 0.1	2.473 ± 0.025	0.100 ± 0.010	−1.413
Fe—Fe/Ni	1.7 ± 0.2	2.924 ± 0.029	0.112 ± 0.011	0.800
Fe—Fe	1.9 ± 0.2	3.446 ± 0.034	0.112 ± 0.011	
Reactivation			FF-range: 1.1–4.2 Å[i] i	
Fe—Fe	2.6 ± 0.1	2.464 ± 0.025	0.087 ± 0.009	8.58
Fe—Fe/Ni	1.2 ± 0.1	2.890 ± 0.029	0.112 ± 0.011	1.06×10^{-6}
Fe—Fe	1.2 ± 0.1	3.533 ± 0.035	0.112 ± 0.011	−4.109
Fe—Fe	0.4 ± 0.1	4.006 ± 0.040	0.059 ± 0.006	0.800
Mar1			FF-range: 1.1–3.6 Å[i]	
Fe—O	0.1 ± 0.1	1.890 ± 0.019	0.032 ± 0.003	16.09
Fe—O	0.3 ± 0.1	2.004 ± 0.020	0.032 ± 0.003	5.44×10^{-6}
Fe—Fe	2.1 ± 0.2	2.495 ± 0.025	0.102 ± 0.010	−6.947
Fe—Fe/Ni	1.1 ± 0.1	3.019 ± 0.030	0.112 ± 0.011	0.800
Fe—Fe	0.8 ± 0.1	3.482 ± 0.035	0.112 ± 0.011	
Mar2			FF-range: 1.1–3.6 Å[i]	
Fe—O	0.8 ± 0.1	1.847 ± 0.018	0.032 ± 0.003	4.00
Fe—O	0.9 ± 0.1	2.010 ± 0.020	0.032 ± 0.003	0.35×10^{-6}
Fe—Fe	0.4 ± 0.1	2.472 ± 0.025	0.032 ± 0.003	−2.927
Fe—Fe/Ni	1.3 ± 0.1	2.943 ± 0.029	0.087 ± 0.009	0.800
Fe—Fe	1.3 ± 0.1	3.469 ± 0.035	0.092 ± 0.009	

[a] Abs: X-ray absorbing atom, and Bs: backscattering atom.
[b] Number of backscattering atoms.
[c] Distance of the absorbing atom from the backscattering atom.
[d] Debye–Waller like factor.
[e] Fit index.
[f] Reduced χ^2.
[g] Fermi energy, which accounts for the shift between theory and experiment.
[h] Amplitude reduction factor.
[i] Range of Fourier-filtering

dination, respectively, both present in Fe_2NiO_4.[38] It should be noted that a discrimination between oxygen and carbon is not possible by EXAFS analysis due to their similar atomic number, meaning a certain amount of carbon originating from a graphite matrix indicated by total scattering cannot be ruled out at this point. In addition, two shells consisting of iron backscatterers are adjusted at distances of 2.9 and 3.5 Å, which are present in Fe_2NiO_4 as well as in a metallic phase. In the inverse spinel structure of Fe_2NiO_4 the octahedrally coordinated positions are occupied by Fe and Ni ions with a ratio of 1:1 and could not be differentiated. To resemble metallic components characteristically, a further iron shell was modelled at 2.5 Å and in case of

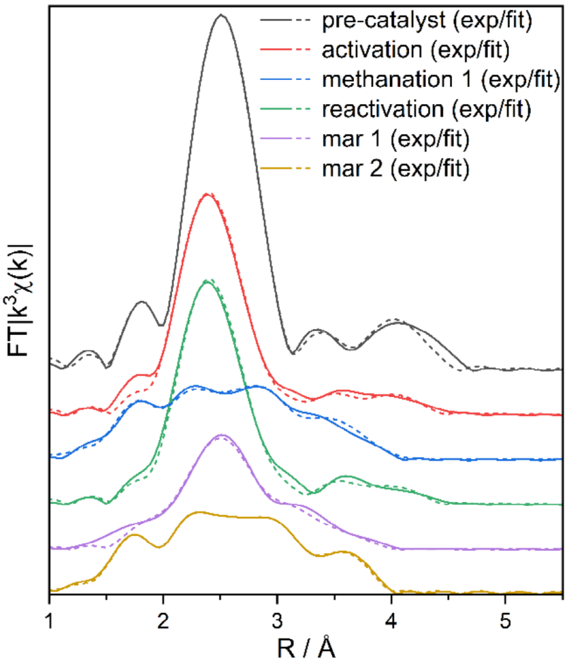

Figure 7. Fourier-transformed EXAFS spectra (Fe K-edge) of the catalyst under investigated conditions.

the pre-catalyst, the activated and reactivated catalysts, also at 4.0 Å.

The spectrum of the pre-catalyst clearly shows a mixture of oxidized components and a metallic phase, due to a pronounced proportion of oxygen backscatterers and a significant amount of Fe backscatterers at 2.48 and 3.97 Å, which can be assigned to Fe^0.[39] This is consistent with the findings in XANES and PDF analysis, where Fe_{bcc} was found. Upon activation, a reduction of the species takes place and the formed Fe phase shows no traces of oxygen backscatterers and a significantly decreased amount of Fe backscatterers at 4.0 Å, which are characteristic for Fe_{bcc}. Due to the very similar backscatterer distances an unambiguous assignment of a possible iron centering cannot be made by EXAFS analysis.[40]

As also visible in the XANES spectra, the catalyst is oxidized to an even higher extent under methanation conditions than in the pre-catalyst, resulting in a higher amount of oxygen backscatterers at 1.914 Å and a significant decrease of Fe backscatterers at 2.473 Å—a characteristic distance for the metallic phase. It is likely that an interaction with the CO_2 from the gas phase takes place, and an in situ species can be observed. The types and distances of the obtained model fit very well to Fe_2NiO_4, which was proposed by PXRD measurements.

In the EXAFS analysis of the seven carried out methanation/full dropout cycles, the weak overall oxidation detectable in XANES analysis cannot be resembled. The applied fits do not show significant changes during the full dropout and methanation cycles (see Figures S11 and S12).

After reactivation, the almost identical structure model could be obtained, as it was used for the activated catalyst. As can be seen in the fits of the spectra after reactivation, the structural changes seem to proceed slower than in the initial catalyst.

The spectrum of the first methanation after reactivation (mar 1) appears to be a mixture of the activated, reduced catalyst and the oxidized one after methanation 1. Only after a second methanation, the spectra resemble those obtained after methanation 1, indicating a higher structural stability.

3. Conclusion

In this paper, we investigated a MOF-derived bimetallic Fe/Ni catalyst during CO_2 methanation in seven catalysis and H_2 dropout cycles by X-ray diffraction and absorption.

During the activation process in pure hydrogen, the Ni/Fe-MOF-derived pre-catalyst was reduced, and the Fe_{bcc} phase was detected by PDF and EXAFS analysis. This Fe_{bcc} phase disappeared when 400 °C was reached, apparently induced by the disintegration of the graphitic shells around the nanoparticles. Some carbon remained in between the particles and created a diffusive scattering background. Neither PDF nor XAS analysis at the Ni K-edge showed any changes in the metallic Ni_{fcc} species formed under all the conditions applied, underlining the stability of the active species obtained.

During full dropout and methanation conditions, the investigated bimetallic catalyst showed exceptional catalytic activity and selectivity in the cycles of methanation and dropouts. Two fcc phases of Ni_3Fe_{fcc} and Ni_{fcc} coexisted, with a Fe_2NiO_4 phase forming continuously during the dropouts possibly on the particle surface, as could be verified by PDF and XAS. Under pure hydrogen atmosphere, the catalyst was fully recovered in the reactivation protocol, as shown by XAS. Correlating the results obtained by X-ray diffraction and absorption spectroscopy with catalytic activity, the presence of the spinal phase Fe_2NiO_4 seemed to stabilize the conversion and product selectivity. Since the spinel phase was depleted during methanation, the catalyst was well suited for full dropout scenarios and pulsed operation.

4. Experimental Section

4.1. Synthesis of $Ni_3Fe(BDC)(PNO)_x$ Precursor and $Ni_3Fe@C$ Catalyst

The synthesis of $Ni_3Fe(BDC)(PNO)_x$ is based on the synthesis of the monometallic material Ni(BDC)(PNO).[41] The nickel precursor was partially replaced by $Fe(NO_3)_3{\bullet}9H_2O$ and the amount of pyridine-*N*-oxide (PNO) was stoichiometrically adjusted to the Ni content. $Ni(NO_3)_2{\bullet}6H_2O$, $Fe(NO_3)_3{\bullet}9H_2O$, benzene-1,4-dicarboxylic acid (H_2BDC), and pyridine-*N*-oxide (PNO) were dissolved in 60 mL of *N*,*N*–dimethylformamide (DMF) in a 100 mL flask. The reaction solution was subsequently heated to 120 °C for 18 h in an oven. The solid green material was separated from the hot suspension, filtered off, washed with DMF and water, and dried for 72 h at 130 °C in air. For the synthesis of $Ni_3Fe@C$ 1 g of the MOF precursor was placed in a tube furnace, which was heated to 500 °C in a reducing atmosphere of 10% H_2 in He using a heating rate of 5 K min^{-1}. After decomposition for 1 h, the sample was cooled to room temperature and slowly exposed to air due to the pyrophoricity of the freshly decomposed sample. The full experimental details and the results of standard characterization techniques can be found elsewhere.[33]

4.2. Catalytic Measurements

Catalytic experiments in a laboratory U-tube reactor. For the CO_2 hydrogenation studies, 40 mg of the $Ni_3Fe@C$ pre-catalyst was diluted in 160 mg of SiC and placed in a stainless-steel U-tube reactor coated with Silconert2000 and activated at 400 °C for 2 h with 2 K min^{-1} in an H_2 atmosphere to generate the active methanation catalyst. Subsequently, the catalyst was heated to the reaction temperature of 425 °C in an N_2 atmosphere. The CO_2 hydrogenation was performed with a volume flow $\dot{V}$ of 60 $mLmin^{-1}$ of stoichiometric gas composition and an additional 6 mL min^{-1} N_2, resulting in a gas composition fraction of $H_2/CO_2/N_2 = 8:2:1$. For the dropout scenarios, the total gas flow was held constant at 66 mL min^{-1} by balancing with N_2. The fractions of H_2 and CO_2 were adjusted as follows: full dropouts with $H_2/CO_2/N_2 = 0:0:1$ and partial dropouts with $H_2/CO_2/N_2 = 2:1:2.5$. The total product gas flow was measured to exclude effects resulting from volume changes due to the reaction stoichiometry. The products were analyzed using an X-STREAM Enhanced XEGP from Emerson with three IR detector channels for CO_2, CH_4, and CO, as well as a TCD detector for H_2 for quantitative analysis. To prevent the condensation of water within the analyzer, a Peltier sample gas cooler TC-MINI 61,111 from Buehler Technologies was used to cool the products to 5 °C. Additionally, a ThermoStar quadrupole mass spectrometer (QMS) from Pfeiffer was used to identify possible side products.

Catalytic experiments at beamlines. Activation was performed by raising the temperature to 400 °C with a heating ramp of 10 °C/min. As soon as the temperature is reached, activation in H_2 (10 mL/min) atmosphere is run for 1 h. Then the setup is put under a helium atmosphere, and the temperature is raised to 425 °C. In analogy to the experiments in the U-tube reactor, methanation and dropout cycles at the synchrotron facilities were run at 425 °C, took 30 min each, and were alternated for several hours. Only the scenario of full dropouts has been investigated because it showed the best catalytic performance in prior laboratory catalytic runs and for the sake of precious synchrotron beamtime. For the PDF experiments, seven methanation and seven dropout cycles were observed, and He was used instead of N_2 as an inert gas in the gas mixture.

The same catalysis conditions were employed for XAS and PDF experiments, yet with different flow cells optimized for the respective scattering technique, see Rohrbach et al.[10] and below.

4.3. X-ray Total Scattering Experiments

Synchrotron total scattering data were acquired at the ID15A beamline at the ESRF in Grenoble with an X-ray energy of 65 keV ($\lambda = 0.1907$ Å) and a beam size of 150 × 150 μm^2. At the beamline, all experiments were carried out in a quartz capillary reactor (outer diameter 1.5 mm, wall thickness 0.05 mm) with heating coils on top and below the capillary. A custom-built gas dosing system of mass flow controllers (Bronkhorst) was used to control the gas flow of He, H_2, and CO_2 with an overall gas flow of 10 $mLmin^{-1}$ while using a catalyst amount of 7–10 mg. Online gas analysis was performed with a ThermoStar quadrupole mass spectrometer (QMS) from Pfeiffer. The catalytic and dropout cycles were alternated every 30 min. Data was measured continuously with 1 s for each detector image and 29 s sleep time after each image to prevent ghosting issues on the Pilatus CdTe 2 M detector. The powder X-ray diffraction (PXRD) patterns were collected over a Q-range of 0.7–30.8 $Å^{-1}$. Radial integration was done with the software xpdtools,[42] PDF calculation with PDFgetX3,[43] and PDF modeling with diffpy-cmi.[44]

4.4. X-ray Absorption Spectroscopy

All experiments were carried out at beamline P65 at DESY (Deutsches Elektronen-Synchrotron) in Hamburg, Germany. The spectra at the Fe K-edge (7112 eV) and Ni K-edge (8333 eV) were collected at the third undulator harmonic using a Si-coated mirror and a Si(111) double crystal monochromator. For energy calibration of the monochromator a Fe resp. Ni foil was used. The measurements were performed with a maximum beam current of 100 mA in continuous mode (180 s/spectrum) by application of a capillary setup heated by a gas blower in fluorescence mode.

4.5. Transmission Electron Microscopy

High-angle angular dark-field scanning TEM (HAADF-STEM) micrographs and STEM-EDX measurements were acquired on a Thermo Fisher/FEI Talos microscope operated at 200 kV and equipped with 4 in-column Super-X detectors, which allow for superior collection efficiency. The convergence angle used was 10.5 mrad, and the probe current was 420 pA. The images were collected on a sample after reduction and after catalysis with full dropouts in a laboratory reactor; it is important to underline that due to the different condition, the sample measured in the in situ set-up can present some differences. The sample was prepared and measured under an inert atmosphere.

Supporting Information

The authors have cited additional references within the Supporting Information.

Author Contributions

L.R. synthesized the samples and did the catalytic tests, supported by W.K. and C.W. F.M. analyzed the PXRD and PDF data. S.S. conducted the in situ XAS study and analyzed the results, together with R.S. M.B. collected and interpreted TEM data. M.B., W.K. and M.Z. conceptually laid out, M.B. and M.Z. led the project. F.M. and S.S. wrote the original manuscript, supported by M.Z., R.S. and M.B. for data discussion and interpretation. All authors revised the manuscript.

Acknowledgments

We acknowledge funding by the Deutsche Forschungsgemeinschaft (DFG, German Research Foundation) via SPP2080 (LU 2246/3–1, BA 4467/8–1 and BA 4467/8–2, KL 2913/1–1 and KL 2913/1–2, ZO 369/2–1 and ZO 369/2–2). We acknowledge beamtime at beamline P65 at PETRA III, DESY (Hamburg, Germany), proposal I-20200879, a member of the Helmholtz Association HGF, as well as beamtime at beamline ID15A at ESRF (Grenoble, France), proposal CH-6069. We gratefully acknowledge Edmund Welter (P65) and Stefano Checchia (ID15A) for support during the beamtime, as well as Benjamin Fahl and, in particular, Nils Prinz for experimental layout of the PDF experiment and data acquisition. M. B. and T. L. acknowledge support from the German Federal Ministry of Education and Research in the framework of the project Catlab (03EW0015A).

Open access funding enabled and organized by Projekt DEAL.

Conflict of Interests

The authors declare no conflict of interest.

Data Availability Statement

The data analyzed for this article are available in a public GitHub repository at https://github.com/Fabio1911/NiFe_MOF_catalyst_paper.git

Keywords: In situ characterization • Metal organic framework • Methanation • PDF • XAS

[1] P. Sabatier, *Chimie. Paris: Imprimerie Gauthier-Villars* **1902**, *134*, 514–516.
[2] S. Rönsch, J. Schneider, S. Matthischke, M. Schlüter, M. Götz, J. Lefebvre, P. Prabhakaran, S. Bajohr, *Fuel* **2016**, *166*, 276–296.
[3] S. Weber, R. T. Zimmermann, J. Bremer, K. L. Abel, D. Poppitz, N. Prinz, J. Ilsemann, S. Wendholt, Q. Yang, R. Pashminehazar, F. Monaco, P. Cloetens, X. Huang, C. Kübel, E. Kondratenko, M. Bauer, M. Bäumer, M. Zobel, R. Gläser, K. Sundmacher, T. L. Sheppard, *ChemCatChem* **2022**, *14*, e202101878.
[4] B. Lü, W. Qi, M. Luo, Q. Liu, L. Guo, *Ind. Eng. Chem. Res.* **2020**, *59*, 12352–12359.
[5] K. O. Otun, X. Liu, D. Hildebrandt, *J. Energy Chem.* **2020**, *51*, 230–245.
[6] B. Qiu, C. Yang, W. Guo, Y. Xu, Z. Liang, D. Ma, R. Zou, *J. Mater. Chem. A* **2017**, *5*, 8081–8086.
[7] G. S. Day, J. Li, E. A. Joseph, P. C. Metz, Z. Perry, M. R. Ryder, K. Page, H.-C. Zhou, *Nanoscale Adv.* **2020**, *2*, 2758–2767.
[8] M. Folkjær, L. F. Lundegaard, H. S. Jeppesen, M. J. Marks, M. S. Hvid, S. Frank, G. Cibin, N. Lock, *Dalton Trans.* **2022**, *51*, 10740–10750.
[9] N. Prinz, S. Strübbe, M. Bauer, M. Zobel, *New J. Chem.* **2023**, *47*, 11623–11635.
[10] L. Rohrbach, S. Strübbe, N. Prinz, C. Wilhelm, P. Müller, M. Nowakowski, A. Schoekel, M. Zobel, M. Bauer, W. Kleist, *SSRN preprint* **2023**, https://doi.org/10.2139/ssrn.4502507.
[11] J. Keating, G. Sankar, T. I. Hyde, S. Kohara, K. Ohara, *Phys. Chem. Chem. Phys.* **2013**, *15*, 8555–8565.
[12] J. R. Gallagher, T. Li, H. Zhao, J. Liu, Y.u Lei, X. Zhang, Y. Ren, J. W. Elam, R. J. Meyer, R. E. Winans, J. T. Miller, *Catal. Sci. Technol.* **2014**, *4*, 3053–3063.
[13] M. A. Gotthardt, R. Schoch, S. Wolf, M. Bauer, W. Kleist, *Dalton Trans.* **2015**, *44*, 2052–2056.
[14] K. S. M. Salih, S. Bergner, H. Kelm, Y.u Sun, A. Grün, Y. Schmitt, R. Schoch, M. Busch, N. Deibel, S. Bräse, B. Sarkar, M. Bauer, M. Gerhards, W. R. Thiel, *Eur. J. Inorg. Chem.* **2013**, *2013*, 6049–6059.
[15] S. J. L. Billinge, *International Tables for Crystallography*, Vol. *H* IUCr, Wiley, **2019**, 649–672, Ch. 5.7.
[16] L. Gamez-Mendoza, M. W. Terban, S. J. L. Billinge, M. Martinez-Inesta, *J. Appl. Crystallogr.* **2017**, *50*, 741–748.
[17] D. Tsymbarenko, D. Grebenyuk, M. Burlakova, M. Zobel, *J. Appl. Crystallogr.* **2022**, *55*, 890–900.
[18] P. J. Chupas, K. W. Chapman, G. Jennings, P. L. Lee, C. P. Grey, *J. Am. Chem. Soc.* **2007**, *129*, 13822–13824.
[19] N. K. Zimmerli, C. R. Müller, P. M. Abdala, *Trends Chem.* **2022**, *4*, 807–821.
[20] A. I. Tsiotsias, N. D. Charisiou, I. V. Yentekakis, M. A. Goula, *Nanomaterials* **2020**, *11*, 28.
[21] B. Mutz, M. Belimov, W. Wang, P. Sprenger, M.-A. Serrer, D.i Wang, P. Pfeifer, W. Kleist, J.-D. Grunwaldt, *ACS Catal.* **2017**, *7*, 6802–6814.
[22] Y.-T. Li, L. Zhou, W.-G. Cui, Z.-F. Li, W. Li, T.-L. Hu, *J. CO_2 Util.* **2022**, *62*, 102093.
[23] H. L. Huynh, J. Zhu, G. Zhang, Y. Shen, W. M. Tucho, Y. Ding, Z. Yu, *J. Catal.* **2020**, *392*, 266–277.
[24] C. Mebrahtu, F. Krebs, S. Perathoner, S. Abate, G. Centi, R. Palkovits, *Catal. Sci. Technol.* **2018**, *8*, 1016–1027.
[25] M.-A. Serrer, A. Gaur, J. Jelic, S. Weber, C. Fritsch, A. H. Clark, E. Saraçi, F. Studt, J.-D. Grunwaldt, *Catal. Sci. Technol.* **2020**, *10*, 7542–7554.
[26] L. P. L. Gonçalves, J. P. S. Sousa, O. S. G. P. Soares, O. Bondarchuk, O. I. Lebedev, Y. V. Kolen'ko, M. F. R. Pereira, *Catal. Sci. Technol.* **2020**, *10*, 7217–7225.
[27] L. Yin, X. Chen, M. Sun, B. Zhao, J. Chen, Q. Zhang, P. Ning, *Int. J. Hydrogen Energy* **2022**, *47*, 7139–7149.
[28] J. Ren, F. Zeng, C. Mebrahtu, Z. Wang, R. Palkovits, *J. Energy Chem.* **2023**, *86*, 351–361.
[29] D. Pandey, G. Deo, *J. Mol. Catal. A: Chem.* **2014**, *382*, 23–30.
[30] Z. Song, Q. Wang, C. Guo, S. Li, W. Yan, W. Jiao, L. Qiu, X. Yan, R. Li, *Ind. Eng. Chem. Res.* **2020**, *59*, 17250–17258.
[31] S. Farsi, W. Olbrich, P. Pfeifer, R. Dittmeyer, *Chem. Eng. J.* **2020**, *388*, 124233.
[32] J. Sehested, K. E. Larsen, A. L. Kustov, A. M. Frey, T. Johannessen, T. Bligaard, M. P. Andersson, J. K. Nørskov, C. H. Christensen, *Top. Catal.* **2007**, *45*, 9–13.
[33] L. Rohrbach, C. Wilhelm, W. Kleist, *ChemRxiv Preprint* **2025**, https://doi.org/10.26434/chemrxiv-2025-3f794.
[34] S. M. Kim, P. M. Abdala, T. Margossian, D. Hosseini, L. Foppa, A. Armutlulu, W. van Beek, A. Comas-Vives, C. Copéret, C. Müller, *J. Am. Chem. Soc.* **2017**, *139*, 1937–1949.
[35] R. W. G. Wyckoff, *Crystal Structures* **1963**, *1*, 7–83.
[36] B. Bieniek, D. Pohl, L. Schultz, B. Rellinghaus, *J. Nanopart. Res.* **2011**, *13*, 5935–5946.
[37] K. Sumiyama, M. Kadono, Y. Nakamura, *Trans. JIM* **1983**, *24*, 190–194.
[38] K. N. Subramanyam, *J. Phys. C: Solid State Phys.* **1971**, *4*, 2266–2268.
[39] E. A. Owen, G. I. Williams, *J. Sci. Instrum.* **1954**, *31*, 49–54.
[40] Y. Nishihara, Y. Nakajima, A. Akashi, N. Tsujino, E. Takahashi, K. Funakoshi, Y. Higo, *Am. Mineral.* **2012**, *97*, 1417–1420.
[41] N. Prinz, L. Schwensow, S. Wendholt, A. Jentys, M. Bauer, W. Kleist, M. Zobel, *Nanoscale* **2020**, *12*, 15800–15813.
[42] C. J. Wright, X. D. Zhou, *J. Synchrotron Radiat.* **2017**, *24*, 506–508.
[43] P. Juhás, T. Davis, C. L. Farrow, S. J. L. Billinge, *J. Appl. Crystallogr.* **2013**, *46*, 560–566.
[44] P. Juhás, C. L. Farrow, X. Yang, K. R. Knox, S. J. L. Billinge, *Acta Crystallogr., Sect. A: Found. Adv.* **2015**, *71*, 562–568.

Manuscript received: May 12, 2025
Revised manuscript received: June 28, 2025
Accepted manuscript online: July 4, 2025
Version of record online: ■■, ■■